metals

MDPI

Article

The Precipitation Behavior in $Al_{0.3}CoCrFeNi$ High-Entropy Alloy Affected by Deformation and Annealing

Jinlong Zhang [1,2], Risheng Qiu [1,*], Xinu Tan [1], Xuantong Quan [1], Bo Song [3,*] and Qing Liu [1,4]

[1] International Joint Laboratory for Light Alloys (MOE), College of Materials Science and Engineering, Chongqing University, Chongqing 400044, China
[2] The 44th Research Institute of CETC, Chongqing 400060, China
[3] School of Materials and Energy, Southwest University, Chongqing 400715, China
[4] Key Laboratory for Light-Weight Materials, Nanjing Tech University, Nanjing 210009, China
* Correspondence: rsqiu@cqu.edu.cn (R.Q.); bosong@swu.edu.cn (B.S.)

Abstract: The effects of deformation and annealing on the precipitation behaviors, including the structure and chemical composition of the $L1_2$, B2, BCC and σ phases, in $Al_{0.3}CoCrFeNi$ high entropy alloy were analyzed. Firstly, the thermodynamic factors controlled the precipitation pathway in as-cast alloys, which led to the $L1_2$ precipitating homogeneously in the FCC matrix under a low annealing temperature, while the B2 precipitated under a high annealing temperature. In contrast, if the deformation was introduced before annealing, the precipitation pathway of the second phase was completely changed to the B2, BCC and σ phases because of the combination of thermodynamic and kinetic conditions. In particular, the B2 and σ phases promoted the precipitation behavior reciprocally due to the complementary chemical compositions. The elaborate precipitation behaviors of the $L1_2$, B2, BCC and σ phases were analyzed to identify the phase transformation in the $Al_{0.3}CoCrFeNi$ HEA. These transformation pathways and elaborate structural features of the $L1_2$, B2, BCC and σ phases provide various design possibilities for the microstructures and properties of single FCC HEAs.

Keywords: $Al_{0.3}CoCrFeNi$; mechanical properties; high-entropy alloy; annealing; 3DAP

Citation: Zhang, J.; Qiu, R.; Tan, X.; Quan, X.; Song, B.; Liu, Q. The Precipitation Behavior in $Al_{0.3}CoCrFeNi$ High-Entropy Alloy Affected by Deformation and Annealing. *Metals* **2023**, *13*, 157. https://doi.org/10.3390/met13010157

Academic Editor: Babak Shalchi Amirkhiz

Received: 21 December 2022
Revised: 5 January 2023
Accepted: 10 January 2023
Published: 12 January 2023

1. Introduction

Generally, the high-entropy alloy (HEA) is recognized as a multi-principal element alloy composed of five or more primary elements [1–5]. Differing from the conventional alloys, the existing HEAs with different microstructures and properties were expected to be applied as structural materials in a range of fields [6,7]. With this intention, the $Al_{0.3}CoCrFeNi$ HEA, with outstanding strength and ductility, was prominent among the many HEAs. In detail, according to the current research, the strength of as-cast$Al_{0.3}CoCrFeNi$ HEA reaches approximately 300 to 400 MPa, while the ductility remains at 60 to 90% [8–11]. To further develop the alloys, the properties of $Al_{0.3}CoCrFeNi$ HEA were modified through deformation and annealing treatment, which primarily introduced dislocation, recrystallization and second-phase transformation [12–15]. Deformation uniformly provided the dislocation for the alloy, which was related to the stacking fault energy [16]. The main deformation methods include rolling, forging, drawing and extrusion [17–20]. In particular, $Al_{0.3}CoCrFeNi$ HEA fibers with diameters ranging from 1 to 3.15 mm were fabricated by hot-drawing, resulting in the tensile strength and ductility of the fibers improving to 1207 MPa and 7.8%, which contributed to the second-phase transformation and texture [18]. Moreover, heat treatment, including the annealing temperature, heating time and cooling rate, normally affects the second-phase precipitation [21,22]. For instance, the strength of $Al_{0.3}CoCrFeNi$ HEA samples reached 1850 MPa after annealing treatment at 1150 °C for 10 h, cold-rolling to 90% thickness reduction and subsequent annealing at 550 for 24 h [23]. In consequence, controlling phase transformation via deformation processes and heat treatment is effective in improving the properties of alloys [24].

Hence, the detailed structural information, chemical composition and precipitation law of the $L1_2$, B2, BCC and σ phases were significant for the advanced development of AlxCoCrFeNi HEA [25–29]. The stable B2 phase enriched in Al and Ni elements was the primary phase in the deformation and annealing treatment process that affected the properties of the AlxCoCrFeNi HEA [24–27]. Moreover, the $L1_2$ phase was normally precipitated in the annealed as-cast AlxCoCrFeNi HEA [23,29–33]. The BCC phase was closely related to the Cr element content, while the σ phase, primarily composed of Cr, Fe and Co elements, had a tetragonal structure. Attributed to the previous research, the AlxCoCrFeNi HEA was combined with remarkable strength and ductility [34–40]. However, for $Al_{0.3}$CoCrFeNi HEA high-entropy alloys, the characteristics of the second phases require further investigation [41]. In consequence, the precipitation behavior of $Al_{0.3}$CoCrFeNi HEA during the deformation and annealing procedure is imperative to study.

In this research, the as-castand rolled $Al_{0.3}$CoCrFeNi HEA was annealed at 500 °C, 540 °C, 590 °C and 660 °C for 24 h and 700 °C and 800 °C for 10 h. The precipitation behavior, microstructure and chemical composition of the $L1_2$, B2, BCC and σ phases were analyzed, intending to research the phase transformation mechanisms in $Al_{0.3}$CoCrFeNi HEA.

2. Materials and Methods

The as-cast $Al_{0.3}$CoCrFeNi HEA was produced by vacuum induction in a melting furnace (LGZ-3, Shenzhen Summit New Materials) with elements of at least 99.9 wt% purity. The metal specimens with dimensions of 40 × 40 × 20 mm^3, cut from AH samples, were cold-rolled with 90% deformation by two high universal mills at Chongqing University. Further, the as-castalloy and 90% rolled alloy were annealed at different temperatures and subsequently air-quenched, which the detailed processing information listed in Table 1. Then, specimens with dimensions of 10 × 7 × 2 mm^3 were cut from the corresponding samples for microstructural analysis. After being mechanically sanded with SiC paper (4000 # in the final step), the samples subjected to a scanning electron microscope (SEM) and transmission electron microscope (TEM) were processed via an electro-polishing process. The AH and AR specimens processed by annealing were characterized by the TESCAN Mira 3 SEM and FEI G2 F20 TEM equipped with an energy-dispersive spectroscopy (EDS) detector. Samples with dimensions of 10 × 7 × 2 mm^3 were prepared and polished, and the LEAP 4000HR three-dimensional atom probe (3DAP) was used to complete the atom probe tomography (APT) analysis.

Table 1. Detailed processing parameters of the samples.

Sample	Processing Treatment
AH	The as-cast sample
AH500	AH sample aged at 500 °C for 24 h
AH540	AH sample aged at 540 °C for 24 h
AH590	AH sample aged at 590 °C for 24 h
AH660	AH sample aged at 660 °C for 24 h
AH700	AH sample aged at 700 °C for 10 h
AH800	AH sample aged at 800 °C for 10 h
AR	AH sample cold-rolled by a thickness reduction of 90%
AR500	AR sample aged at 500 °C for 24 h
AR540	AR sample aged at 540 °C for 24 h
AR590	AR sample aged at 590 °C for 24 h
AR660	AR sample aged at 660 °C for 24 h
AR700	AR sample aged at 700 °C for 10 h
AR800	AR sample aged at 800 °C for 10 h

3. Results and Discussion

3.1. Precipitation in AH Samples

The SEM image of the as-cast$Al_{0.3}$CoCrFeNi HEA is shown in Figure 1a. The average size of the original grains was roughly 340 μm. Figure 1b exhibits the bright-field (BF)

image of the AH sample. Apparently, the matrix of the sample was relatively homogeneous, without a second phase, and dislocation lines were observed in the grains. Figure 1c is the selected area diffraction pattern (SADP) from the [110] zone axis (ZA), which accounts for the face-centered cubic (FCC) structure of the as-castalloy.

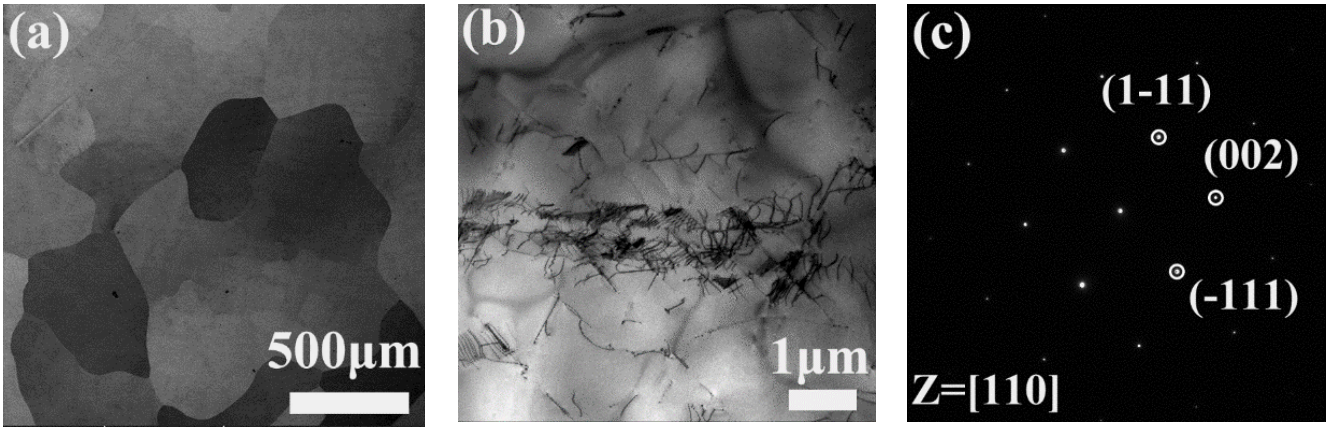

Figure 1. SEM and TEM images of as-cast$Al_{0.3}$CoCrFeNi high-entropy alloy: (**a**) BSE image; (**b**) BF image; (**c**) SADP image.

Figure 2 exhibits the dark-field images and SADP image of AH samples. After annealing at 500 °C, 540 °C, 590 °C, 660 °C and 700 °C, $L1_2$ precipitates were observed in the samples. As the annealing temperature was raised, the scales of the $L1_2$ phase in the AH500, AH540, AH590, AH660 and AH700 samples were measured to be roughly 1 nm, 2 nm, 5 nm, 10 nm and 20 nm, respectively. Figure 2f is the SADP image of the AH590 sample, which represents the FCC structures of both matrix and $L1_2$ precipitation from the [110] FCC ZA. The white circles in Figure 2f indicate the diffraction spots of the matrix. The small spot circled by red lines represents the $L1_2$ phase. In Figure 2g, the SADP image of the [100] FCC ZA of the AH700 sample shows the fundamental reflections of the matrix and extra spots of the $L1_2$ phase. Furthermore, Figure 2h shows the high-resolution scanning TEM image with the corresponding SADP calculated by the Fast Fourier Transform (FFT) method from the [110] FCC condition. In Figure 2i, the region indicated by the white dashed line was acquired through FFT and inverse FFT methods. The white dashed line in Figure 2i identifies the interface of the matrix and $L1_2$ precipitate distinctly. Combined with the extra diffraction spots and high-resolution TEM image of the interface, the $L1_2$ phase separated out from the matrix was ordered and coordinated with the FCC matrix. Moreover, the formation principle of the FCC $L1_2$ phase was mainly driven by the limited thermal conditions at a low annealing temperature.

The 3DAP results and corresponding element concentration curves of the Al, Co, Cr, Fe and Ni elements between the matrix and $L1_2$ phase at atomic percentages from the AH590 and AH660 samples are exhibited in Figure 3. Respectively, Figure 3a,c show the 3DAP reconstruction images of the $L1_2$ phase in AH590 and AH660 samples. The $L1_2$ phase particles were uniformly distributed in the FCC matrix, generally with an irregular ellipsoid shape. Significantly, the size of the $L1_2$ phase increases, while the density decreases, as the annealing temperature increases. Figure 3b,d reveal that the size of $L1_2$ precipitates in AH590 is smaller than 2 nm, while that in the AH700 sample is roughly 9 nm.

Figure 4 exhibits the TEM images with corresponding SADP of the AH800 sample. A large number of particles with different morphologies can be observed in Figure 4a. The B2 phase was a body-centered cubic (BCC) structure with the lattice parameter a = 0.294 nm. The round and acicular B2 precipitates are indicated by a red arrow in Figure 4a. Figure 4b exhibits a 100-nm-scale B2 phase observed from the [110] B2 ZA with an element composition of Al = 10.24% and Ni = 34.62%. Specifically, the red dashed line represents the B2 phase, while the white dashed line represents the FCC matrix in Figure 4c,d. Apparently,

the {111} lattice plane of FCC is parallel to {110} B2, while the {011} FCC is parallel to {111} B2, indicated by the red dashed arrow in Figure 4c,d. In consequence, the Kurdjumov-Sachs (K-S) relationship between the B2 phase and FCC matrix existed in the AH samples annealed at 800 °C for 10 h [29,41–43]. In addition, the high annealing temperature can provide sufficient energy for the transference of Al and Ni elements, resulting in the formation of the more stable B2 phase [6,44,45].

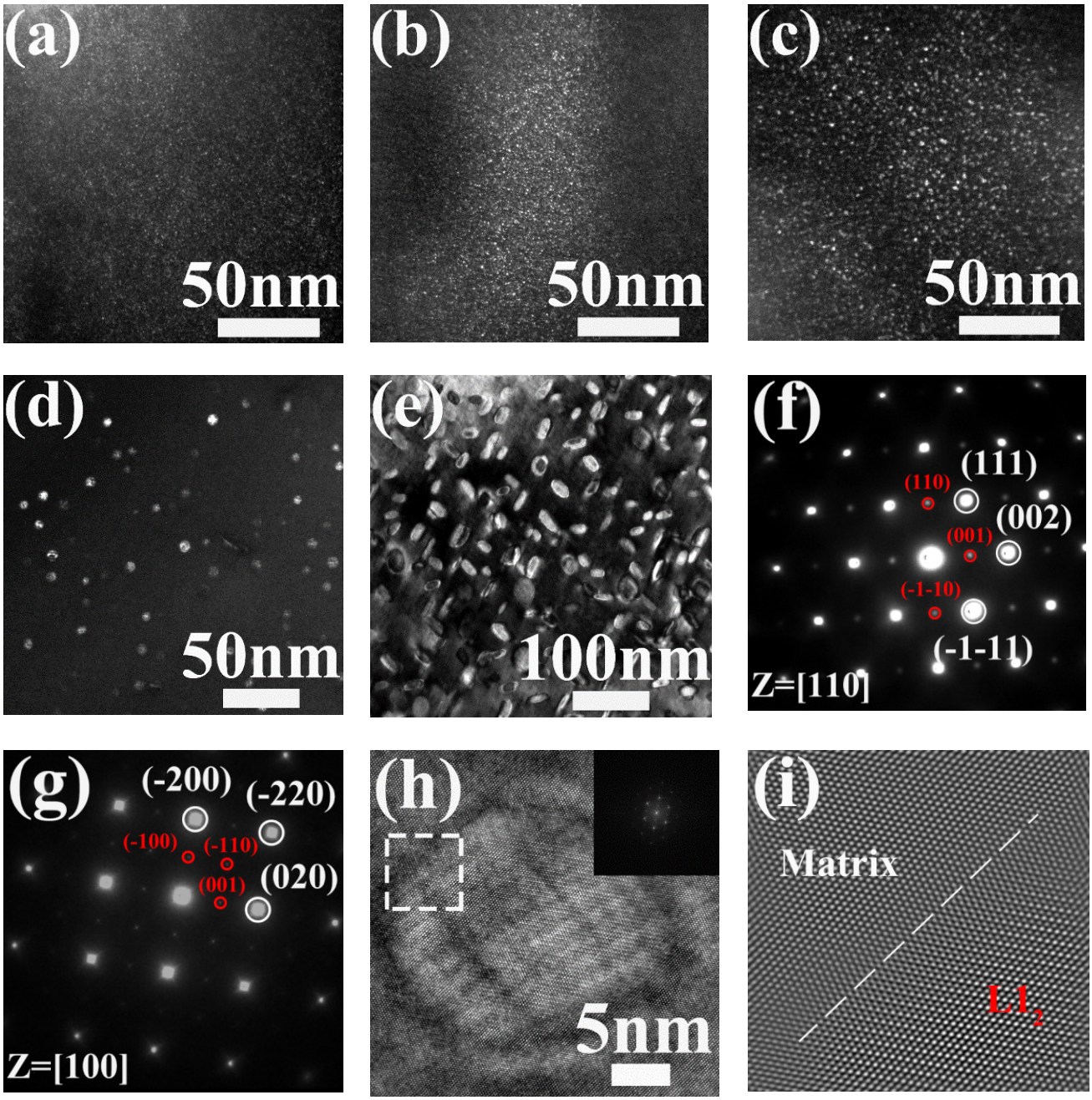

Figure 2. TEM images and corresponding SADP of $L1_2$ phase in annealed as-cast$Al_{0.3}$CoCrFeNi high-entropy alloy: (**a**) AH500 sample; (**b**) AH540 sample; (**c**) AH590 sample; (**d**) AH660 sample; (**e**) AH700 sample; (**f**) SADP of AH590 sample; (**g**) SADP of AH700 sample; (**h**,**i**) high-resolution scanning TEM images of $L1_2$ in AH700.

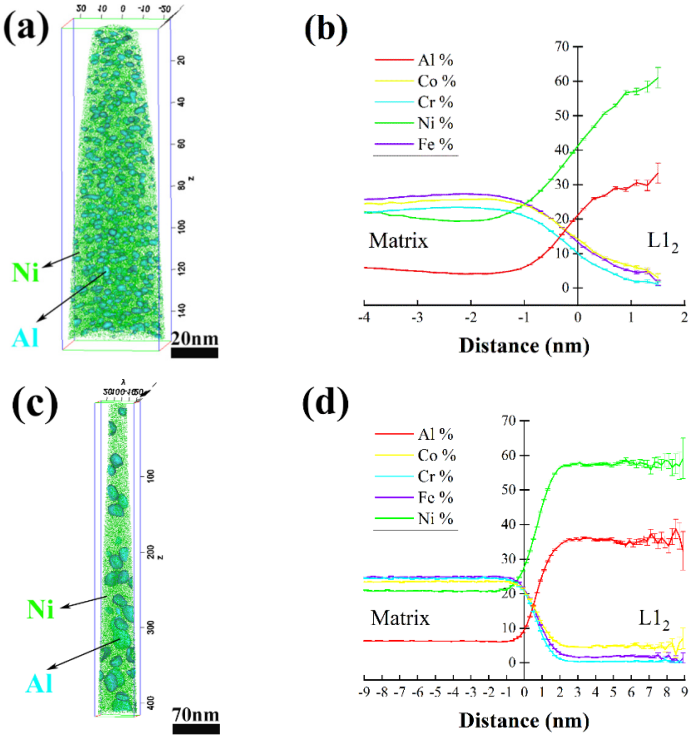

Figure 3. The 3DAP reconstruction images and corresponding concentrations of Al, Co, Cr, Fe and Ni elements between matrix and $L1_2$ phase at atomic percentage: (**a**,**b**): AH590 sample; (**c**,**d**): AH700 sample.

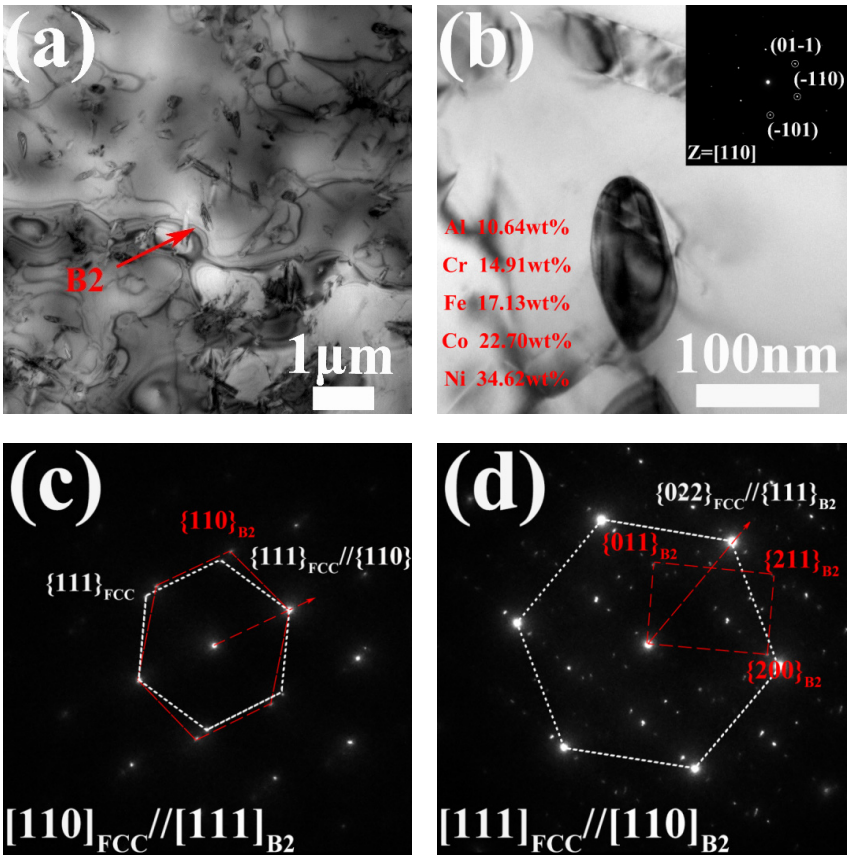

Figure 4. TEM images and corresponding SADP of B2 phase in AH800 sample: (**a**,**b**) BF images of B2 phase; (**c**,**d**) SADP of B2 phase and matrix.

3.2. Precipitation in AR Samples

After annealing at 500 °C, 540 °C, 590 °C, 660 °C, 700 °C and 800 °C, B2 precipitations were observed in the entirety of the AR samples. The B2 precipitates in AR samples were generally circular, as compared to the acicular morphologies in AH800 samples. The size of the B2 particles in AR samples was affected by the annealing temperature. In Figure 5a, the diameter of B2 precipitates of the AR500 sample is roughly 100 nm, while in Figure 5f, the B2 precipitates in the AR800 sample are larger than 200 nm. Moreover, the images of the B2 precipitates shown in Figure 5 were uniformly acquired from the [111] B2 and [110] B2 ZA, which represent the BCC lattice structure. In addition, the lattice parameter for B2 precipitates is 0.294 nm, calculated by the corresponding SADP. In Figure 5g,h, the white and red lines indicate the SADP of the FCC structural matrix and BCC structural B2 phase in the AR660 sample, respectively. As shown by the red arrow, the {111} FCC was parallel to {110} B2, and the {011} FCC was parallel to {111} B2. Clearly, there is a K-S relationship between the B2 phase and matrix [29,43].

Figure 6 shows the Al element EDS images of annealed AR samples. The density of the B2 phase increased as the annealing temperature was raised from 500 °C to 800 °C. In Figure 6a–c, the size of the B2 precipitation is still small. As the temperature increased to 660 °C, the size and quantity of the B2 phase apparently increased, accompanied by the more obvious segregation of the Al element, shown in Figure 6d. Compared with the AH samples, the B2 phase in AR samples was separated out at the temperatures of 500 °C to 800 °C, rather than only in the AH800 sample. Moreover, the size of B2 precipitation in the AR800 sample was primarily larger than 200 nm, while the size of B2 in the AH800 sample was roughly less than 100 nm. The differences in the phase transformation were related to the rolling procedure, which provides more energy for the concentration discrepancy of the Al element in AR samples. The Al element was more inclined to promote the formation of the BCC structural B2 phase to further replace the FCC matrix or $L1_2$ phase. Because of their larger size, the Al atoms among the Al, Co, Cr, Fe and Ni elements in the rolled HEA were forced to adopt the BCC structure due to the large size discrepancy within the FCC lattice [25,46–48].

Figure 7 exhibits the TEM images and corresponding SADP of the BCC phase in AR500, AR540 and AR590 samples. The size of the BCC precipitates of the AR500 sample in Figure 7a is roughly 100 nm, while the BCC precipitates of AR540 and AR590 specimens were above 200 nm, as shown in Figure 7b,c. As the annealing temperature was raised, the diameter of BCC precipitation was increased. In addition, Figure 7d shows the corresponding SADP of the BCC phase in the AR540 sample, which was acquired from the [111] BCC ZA. In consequence, the BCC phase had a uniform BCC structure. After calculation, the lattice parameter of the BCC phase was 0.296 nm. The chemical composition of BCC precipitation is indicated in red in Figure 7a–c. The Cr element content of the BCC phase in AR500, AR540 and AR590 samples was 80.75%, 89.07% and 83.54% at weight percentage, respectively.

Figure 8 shows the TEM images and corresponding SADP of the σ phase in AR samples annealed at 540 °C, 590 °C, 660 °C, 700 °C and 800 °C. In AR540 and AR590 samples, the σ precipitates were separated out from the FCC matrix independently. When the annealing temperature was raised, the σ phase highlighted by the red arrow was precipitated, cooperating with other phases in the cluster that is shown in Figure 8c–e. In addition, the size of σ precipitation in AR540 and AR590 samples was roughly 100 nm. Due to the increment in annealing temperature, the diameter of σ precipitates in AR660, AR700 and AR800 samples was clearly more than 200 nm. Thus, the size of the σ phase was increased as the temperature rose. Based on the corresponding SADP in Figure 8a–e, acquired from [011], [012], [1−20], [0−10] and [001] ZA, respectively, the σ precipitation was able to be certified as a tetragonal structure phase. Figure 8f exhibits the high-resolution scanning TEM image acquired from [111] ZA. In Figure 8a, additional diffraction spots as the (211) and (033) lattice crystal face were observed in the SADP from [011] ZA. Calculated by the FFT and inverse FFT methods, the processed high-resolution image indicated by

the white arrow further revealed the ordered tetragonal structure of the σ phase according to the (011) lattice plane displayed by the red dashed line. Intending to organize the chemical composition, the EDS information about σ precipitation was measured. Normally, the σ phase was enriched in Cr, Fe and Co elements. In the AR540 sample, the element composition of Cr, Fe and Co was 44.64%, 10.09% and 8.93% at weight percentage. In addition, the concentrations of Cr, Fe and Co elements in AR590, AR660, AR700 and AR800 were similar. The higher content of Al and Ni elements in the AR500 sample was attributed to the low annealing temperature, which restricted the atomic migration of Al and Ni.

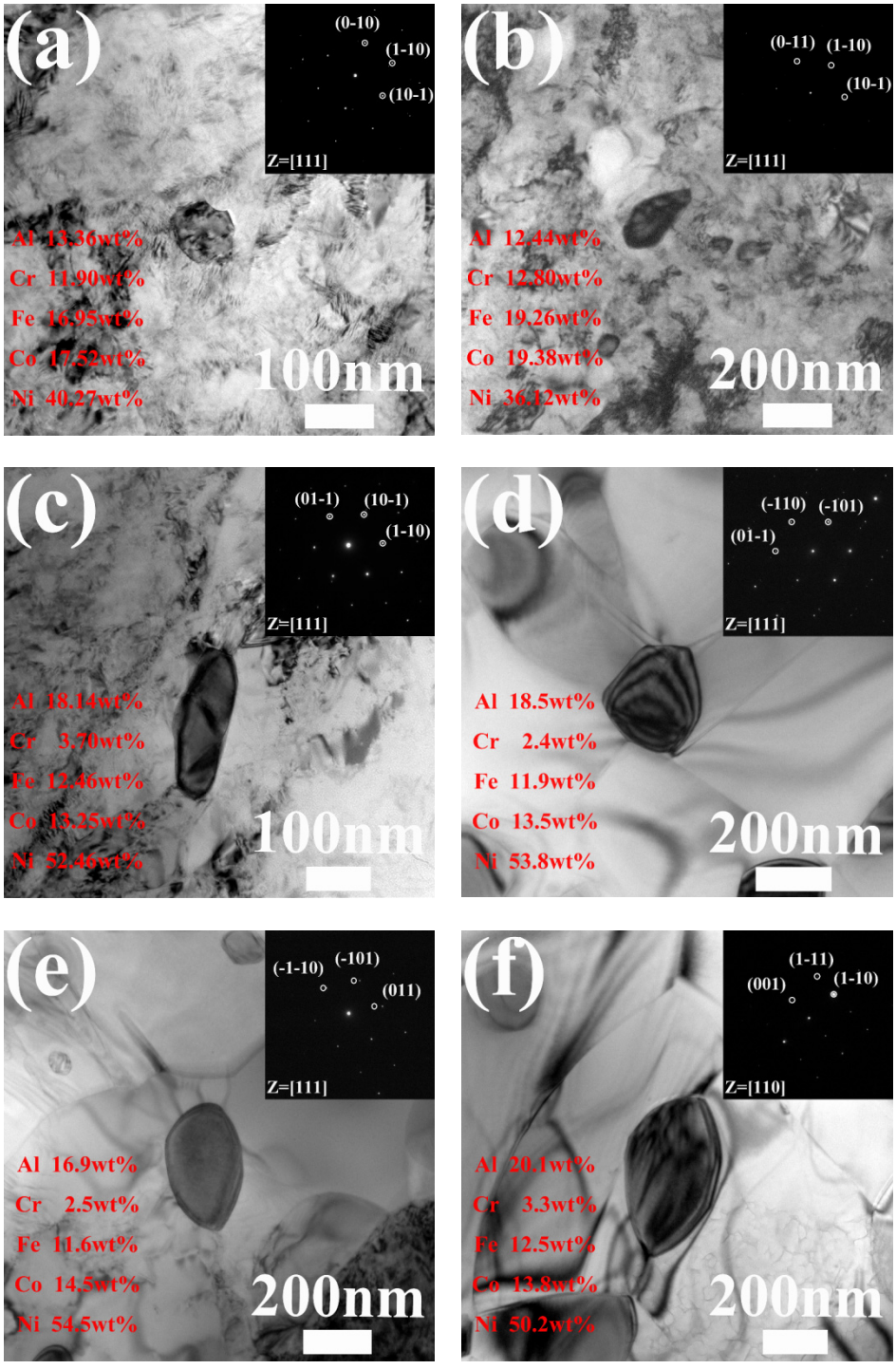

Figure 5. *Cont.*

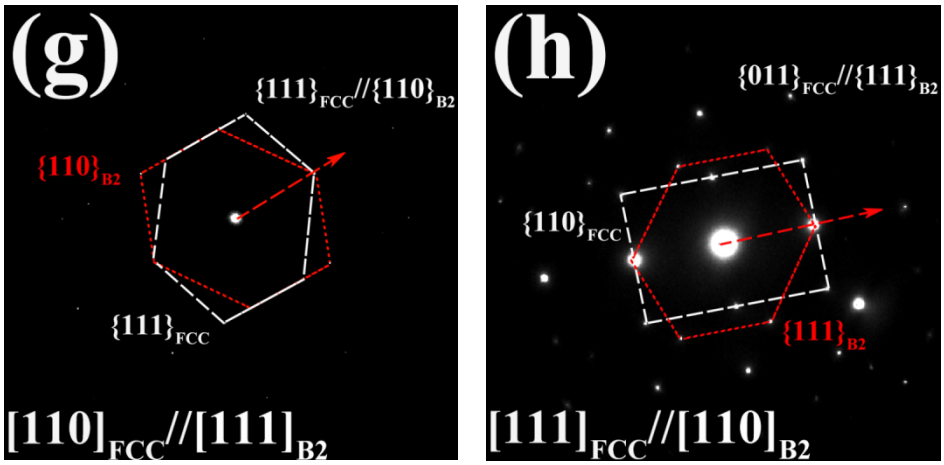

Figure 5. TEM images and corresponding SADP of B2 phase in 90% rolled and annealed samples: (**a**) AR500 sample; (**b**) AR540 sample; (**c**) AR590 sample; (**d**) AR660 sample; (**e**) AR700 sample; (**f**) AR800 sample; (**g**,**h**) SADP of B2 phase and matrix in AR660 sample.

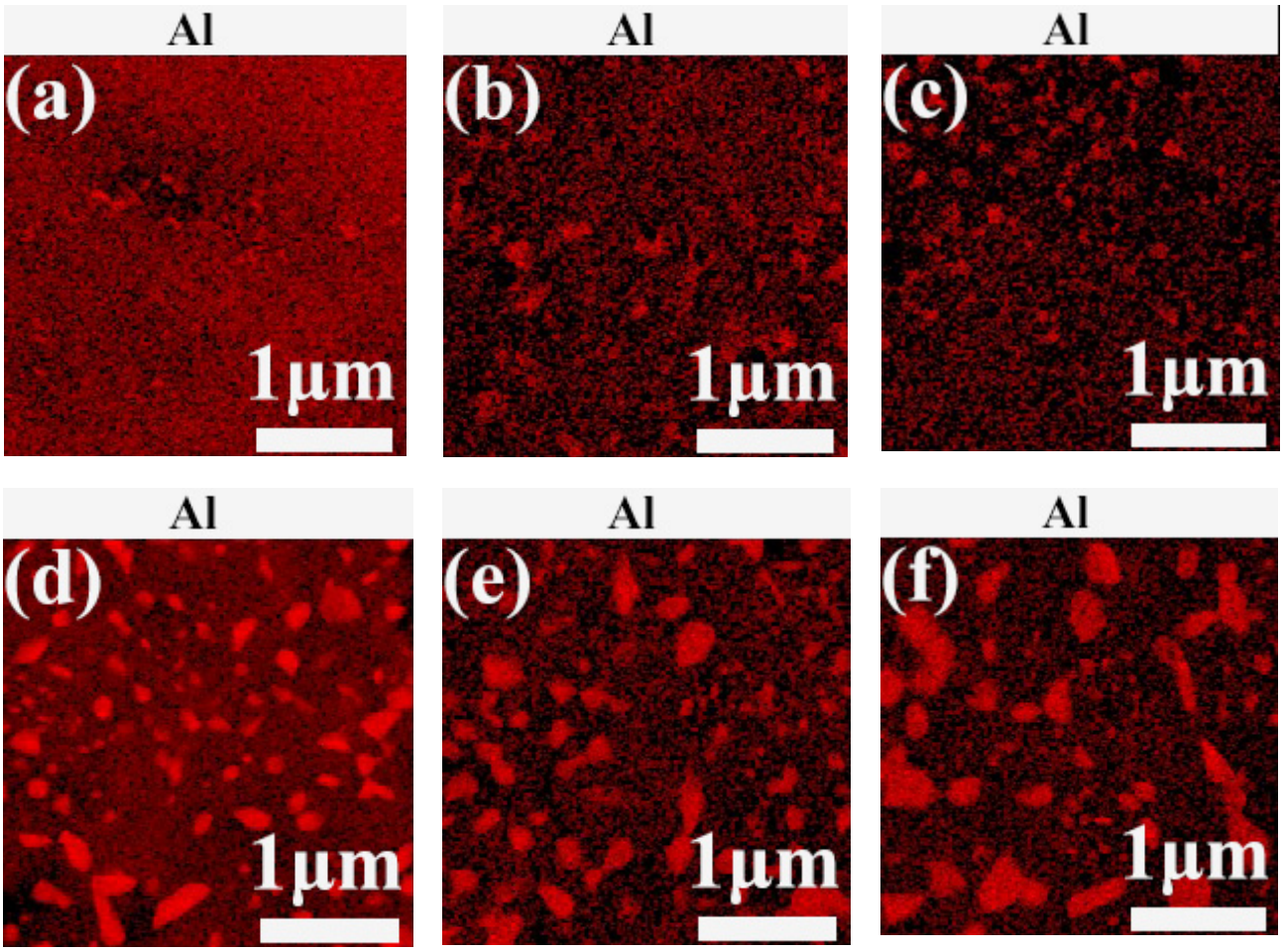

Figure 6. Al elemental energy spectrum mappings of AR samples: (**a**) AR500 sample; (**b**) AR540 sample; (**c**) AR590 sample; (**d**) AR660 sample; (**e**) AR700 sample; (**f**) AR800 sample.

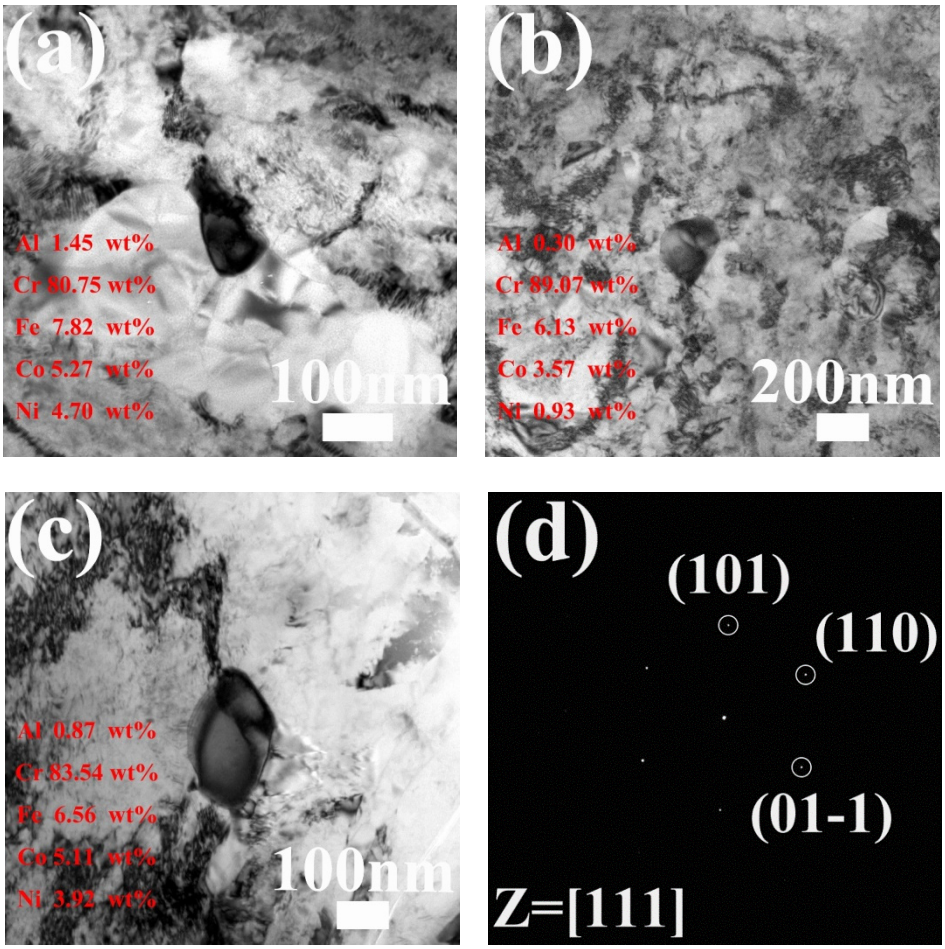

Figure 7. TEM images and corresponding SADP of BCC phase in AR samples: (**a**) AR500 sample; (**b**) AR540 sample; (**c**) AR590 sample; (**d**) corresponding SADP of BCC precipitation in AR540 sample.

Intending to further analyze the precipitation behavior of the second-phase cluster, elemental energy spectrum mappings of the AR660 sample were acquired. Figure 9a–c demonstrate the Al, Ni and Cr elemental energy spectrum mappings. The B2 and σ precipitates are indicated by the red arrow in Figure 9b,c. In the adjacent position of the σ phase, the B2 precipitates were precipitated. The B2 phase was enriched in Al and Ni elements, while the σ phase was enriched in Cr, Fe and Ni elements. In consequence, the complementary chemical compositions of the B2 and σ phases were able to account for the precipitation behavior between the σ and B2 phases. From a chemical perspective, the generation of B2 precipitates would provide Al and Ni deficiency conditions in the surrounding region that results in the improvement of the proportion of Cr, Fe and Co elements, which is conducive to the formation of the σ phase. Hence, around the σ phase, a group of B2 precipitates were separated out in the AR660 sample, as shown in Figure 9a–c. Combined with the previous images in Figure 8c–e, the precipitation performance of the σ and B2 phases possesses mutual promotion in the high-temperature annealed samples. In advance, to further research the relationship among the B2 phase and σ phase at a low annealing temperature, the 3DAP images of the B2 and σ precipitates in the AR590 sample were established. Figure 9d exhibits the reconstruction images of B2 and σ precipitation. Figure 9e shows the σ precipitate in the Cr element atmosphere. The size of the σ precipitate was roughly 5 nm, with a large amount of B2 precipitates produced in the surrounding region. The size of these B2 precipitates was uniformly less than 20 nm. Apparently, the promotion relationship of the B2 and σ phase was still effective in the AR590 sample. Specifically, Figure 9f,g show the element concentration curves of the B2 and σ phase in

the AR590 sample at atomic percentage. The Ni and Al content of B2 precipitates reached 60% and 40% roughly, while the Ni and Al element concentrations in the outside were approximately 20% and 5%, as shown in Figure 9f. On the contrary, the Cr element in the σ phase content approached 50%, as displayed in Figure 9g. Compared with the outside region of B2, the Ni and Al elements in the outside area of the σ phase reached 30% and 10%, which was naturally higher. In consequence, the matrix approaching the σ phase contained a comparatively higher proportion of Al and Ni elements, which provided preferential conditions for the B2 phase. In addition, the content of Cr, Fe and Co elements in the outside region of B2 was roughly 25%, while the content outside of the σ phase was around 20%. The complementary chemical composition of the B2 and σ phases was promoted mutually in the process of precipitation.

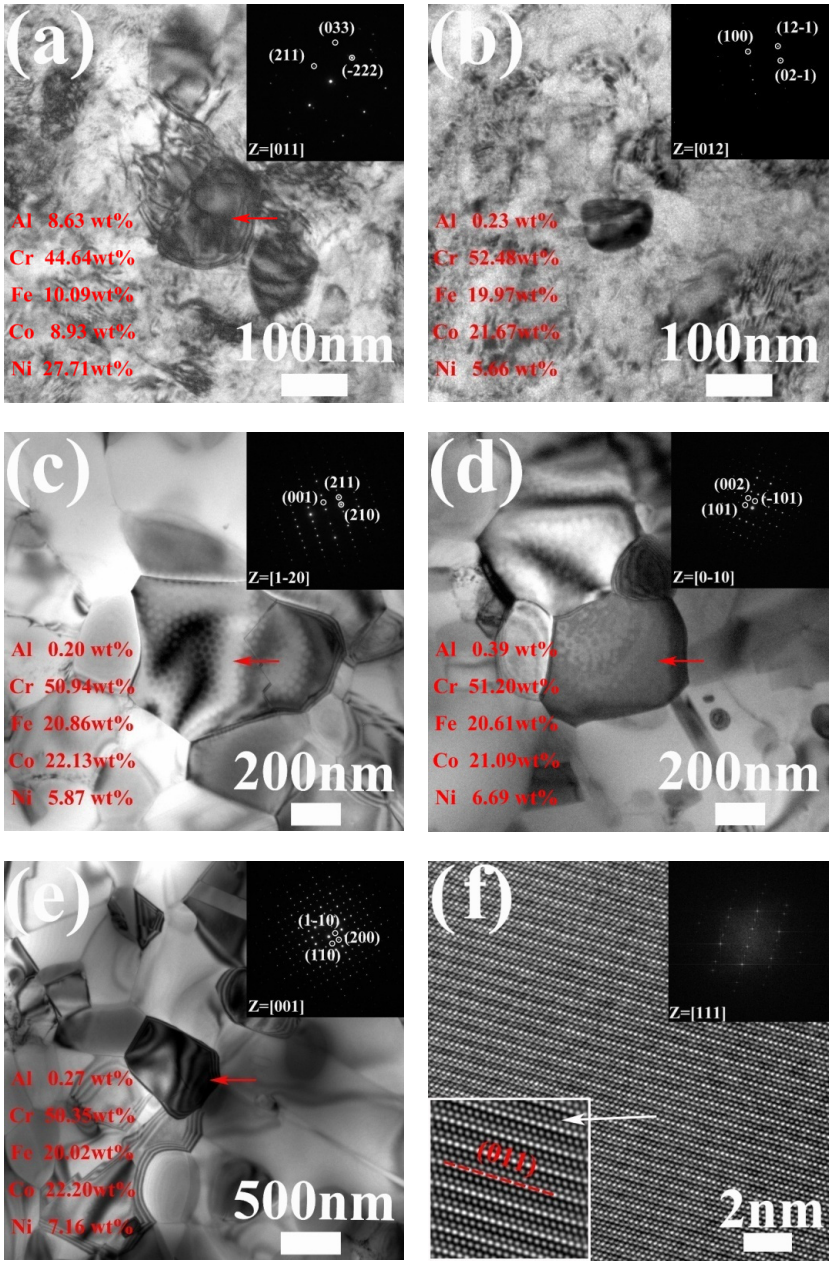

Figure 8. TEM images and corresponding SADP of σ phase in AR samples: (**a**) AR540 sample; (**b**) AR590 sample; (**c**) AH660 sample; (**d**) AR700 sample; (**e**) AR800 sample; (**f**) high-resolution scanning TEM image of σ in AR800.

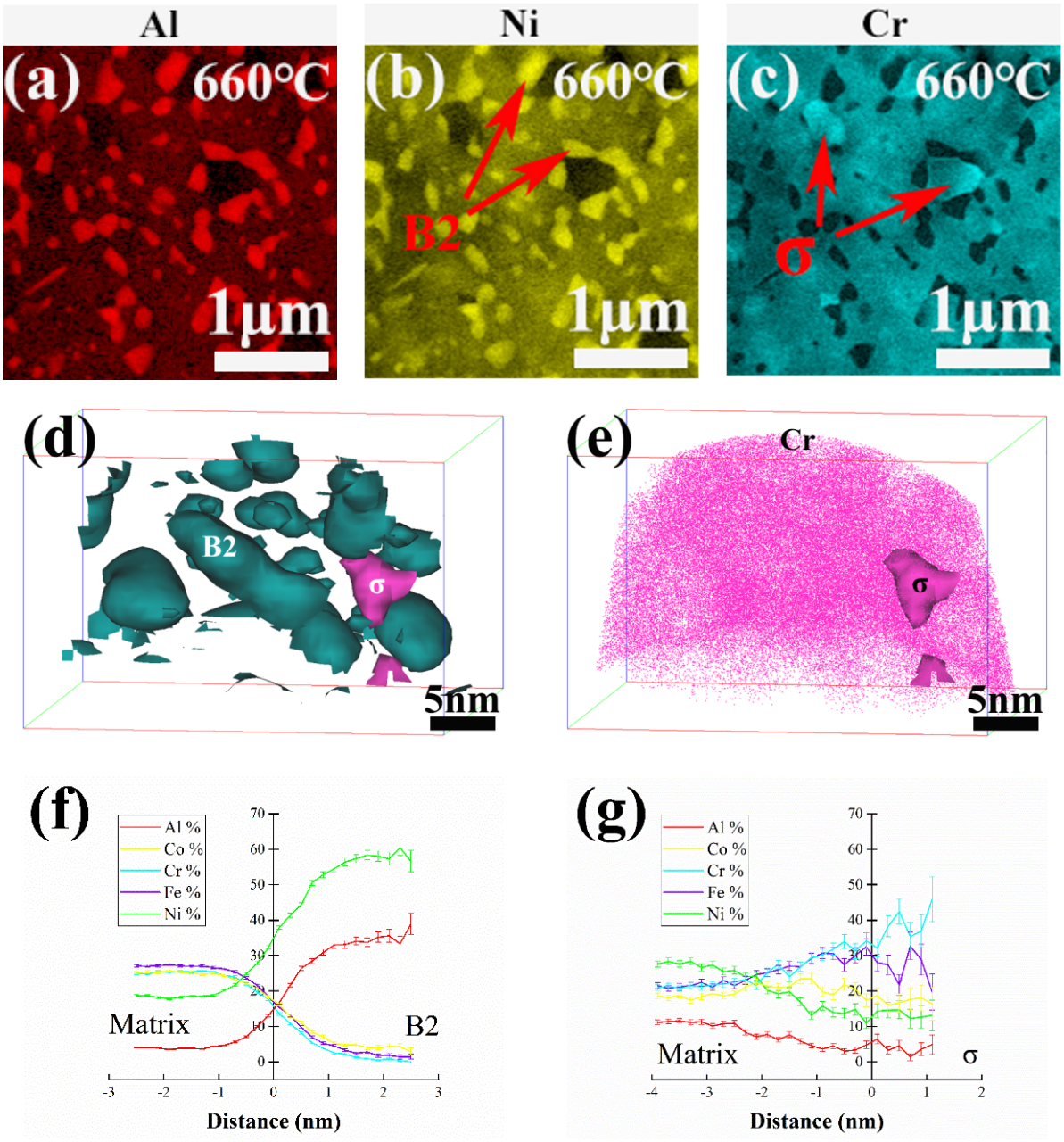

Figure 9. Elemental energy spectrum mappings of AR660 sample and 3DAP reconstruction images with corresponding concentration curves of Al, Co, Cr, Fe, Ni elements of B2 and σ phase in AR590 sample: (**a**–**c**) Al, Ni, Cr elemental energy spectrum mappings of AR660 sample; (**d**,**e**) 3DAP reconstruction images of B2 and σ in AR590 sample; (**f**) element concentration curves of B2 phase and matrix in AR590 sample at atomic percentage; (**g**) element concentration curves of σ phase and matrix in AR590 sample at atomic percentage.

In addition, a difference in precipitates in the AH and AR samples existed. According to the results, the deformation treatment produced an environment for the generation of the B2, BCC and σ phases. The B2 phase with rigid BCC construction was the most precipitated phase in the annealed AH800 and AR samples. In particular, the BCC and σ phases were only discovered in the AR samples. In addition, the starting condition including the AH and AR state of the alloy is the most important factor for the type of precipitation, which was proven to involve the competition between the thermodynamic driving force and activation barrier for second-phase nucleation [49].

4. Conclusions

The AH and AR samples were prepared by annealing and deformation to research the second phase transformation in the $Al_{0.3}CoCrFeNi$ high entropy alloy. According to the TEM and 3DAP technologies, the precipitation characteristics of the $L1_2$, B2, BCC and σ phases were compared and analyzed. The main conclusions are as follows:

(1) The $L1_2$ phase precipitated in the AH samples heated at 500 °C, 540 °C, 590 °C, 660 °C and 700 °C was of the ordered FCC structure and coordinated with the FCC matrix. As analyzed from the 3DAP results, as the annealing temperature was raised from 590 °C to 700 °C, the size of the $L1_2$ phase increased from 2 nm to 9 nm, while the chemical composition was almost invariable.

(2) The B2 phase primarily composed of Al and Ni was of the BCC structure with a lattice diameter a = 0.294 nm, which was discovered in AH800 and all annealed AR samples. The BCC phase enriched in Cr and produced in the AR samples annealed at 500 °C, 540 °C and 590 °C was of the BCC structure with a lattice diameter a = 0.296 nm. The σ phase enriched in Cr, Fe and Co and observed in the 540 °C, 590 °C, 660 °C, 700 °C and 800 °C annealed AR samples was of a tetragonal structure.

(3) The B2 and σ phases, with complementary chemical compositions, promoted the precipitation behavior reciprocally.

Author Contributions: Conceptualization, R.Q. and Q.L.; formal analysis, R.Q.; funding acquisition, R.Q.; investigation, J.Z., X.T. and X.Q.; methodology, R.Q.; project administration, R.Q.; supervision, R.Q.; writing—original draft, J.Z. and B.S.; writing—review and editing, R.Q. and B.S. All authors have read and agreed to the published version of the manuscript.

Funding: The work was supported by the National Natural Science Foundation of China (Grant No. 51421001) and the "111" Project (B16007) of the Ministry of Education and the State Administration of Foreign Expert Affairs of China.

Conflicts of Interest: The authors declare no conflict of interest.

References

1. Miracle, D.; Senkov, O.A. critical review of high entropy alloys and related concepts. *Acta Mater.* **2017**, *122*, 448–511. [CrossRef]
2. Cantor, B.; Chang, I.; Knight, P.; Vincenta, J.B. Microstructural development in equiatomic multicomponent alloys. *Mater. Sci. Eng. A* **2004**, *375–377*, 213–218. [CrossRef]
3. Shen, J.; Agrawal, P.; Rodrigues, T.; Lopes, J.; Schell, N.; Zeng, Z.; MiShra, R.; Oliverira, J.P. Gas tungsten arc welding of as-cast AlCoCrFeNi2.1 eutectic high entropy alloy. *Mater. Des.* **2022**, *223*, 111176. [CrossRef]
4. Martin, A.; Oliveira, J.; Fink, C. Elemental Effects on Weld Cracking Susceptibility in $Al_xCoCrCu_yFeNi$ High-Entropy Alloy. *Metall. Mater. Trans. A* **2020**, *51*, 778–787. [CrossRef]
5. Yasuda, H.Y.; Shigeno, K.; Nagase, T. Dynamic strain aging of $Al_{0.3}CoCrFeNi$ high entropy alloy single crystals. *Scr. Mater.* **2015**, *108*, 80–83. [CrossRef]
6. Zhang, Y.; Zuo, T.T.; Tang, Z.; Gao, M.; Dahmen, K.A.; Liaw, P.K.; Lu, Z. Microstructures and properties of high-entropy alloys. *Prog. Mater. Sci.* **2014**, *61*, 1–93. [CrossRef]
7. Lu, Y.; Dong, Y.; Guo, S.; Jiang, L.; Kang, H.; Wang, T.; Wen, B.; Wang, Z.; Jie, J.; Gao, Z. A Promising New Class of High-Temperature Alloys: Eutectic High-Entropy Alloys. *Sci. Rep.* **2014**, *4*, 6200. [CrossRef] [PubMed]
8. Sun, Y.; Tian, X.; Wei, Y.; Zhuang, Y. Effect of heat treatment on microstructure and mechanical properties of $Al_{0.3}CoCrFeNi$ high entropy alloy with cold rolling. *Trans. Mater. Heat Treat.* **2017**, *18*, 2409–2414.
9. Huang, Y.; Tang, Q.; Dai, P. Effects of Rolling Deformation on Microstructure and Properties of $Al_{0.3}CoCrFeNi$ High-Entropy Alloy. *Mater. Mech. Eng.* **2015**, *39*, 51–54.
10. Gwalani, B.; Soni, V.; Lee, M.; Mantri, S.; Banerjee, R. Optimizing the coupled effects of Hall-Petch and precipitation strengthening in a $Al_{0.3}CoCrFeNi$ high entropy alloy. *Mater. Des.* **2017**, *121*, 254–260. [CrossRef]
11. Gangireddy, S.; Gwalani, B.; Mishra, R. Grain Size Dependence of Strain Rate Sensitivity in a single phase FCC High Entropy Alloy $Al_{0.3}CoCrFeNi$. *Mater. Sci. Eng. A* **2018**, *736*, 344–348. [CrossRef]
12. Ma, L.; Gao, Z.; Hu, S.; Zeng, Z. Effect of cooling rate on microstructure and mechanical properties of $Al_{0.3}CoCrFeNi$ high-entropy alloy. *Mater. Res. Express* **2019**, *6*, 056540. [CrossRef]
13. Kireeva, I.; Chumlyakov, Y.; Pobedennaya, Z.; Vyrodova, A.; Kuksgauzen, I.V.; Kuksgauzen, D.A. Orientation and temperature dependence of a planar slip and twinning in single crystals of $Al_{0.3}CoCrFeNi$ high-entropy alloy. *Mater. Sci. Eng. A* **2018**, *737*, 47–60. [CrossRef]

14. Annasamy, M.; Haghdadi, N.; Taylor, A.; Hodgson, P.; Fabijanic, D. Dynamic recrystallization behaviour of AlxCoCrFeNi high entropy alloys during high-temperature plane strain compression. *Mater. Sci. Eng. A* **2018**, *745*, 90–106. [CrossRef]
15. Jiao, Z.; Ma, S.; Yuan, G.; Wang, H.; Qiao, J. Plastic Deformation of $Al_{0.3}$CoCrFeNi and AlCoCrFeNi High-Entropy Alloys Under Nanoindentation. *J. Mater. Eng. Perform.* **2015**, *24*, 3077–3083. [CrossRef]
16. Zhang, Y.; Lin, J.; Wang, J.; Wang, Y.; Kou, H.; Beaugnon, E. Temperature dependent deformation mechanisms of $Al_{0.3}$CoCrFeNi high-entropy alloy, starting from serrated flow behavior. *J. Alloys Compd. Interdiscip. J. Mater. Sci. Solid-State Chem. Phys.* **2018**, *757*, 39–43. [CrossRef]
17. Zhang, L.; Yu, P.; Cheng, H.; Zhang, H.; Diao, H.Y.; Shi, Y.; Chen, B.L.; Chen, P.; Feng, R.; Bai, J.; et al. Nanoindentation Creep Behavior of an $Al_{0.3}$CoCrFeNi High-Entropy Alloy. *Metall. Mater. Trans. A* **2016**, *47*, 5871–5875. [CrossRef]
18. Li, D.; Li, C.; Feng, T.; Zhang, Y.D.; Sha, G.; Lewandowski, J.; Liaw, P.K.; Zhang, Y. High-entropy $Al_{0.3}$CoCrFeNi alloy fibers with high tensile strength and ductility at ambient and cryogenic temperatures. *Acta Mater.* **2017**, *123*, 285–294. [CrossRef]
19. Xia, Z.; Zhang, M.; Zhao, Y.; Liaw, P.K.; Qiao, J. Effects of Ni-P amorphous films on mechanical and corrosion properties of $Al_{0.3}$CoCrFeNi high-entropy alloys. *Intermetallics* **2018**, *94*, 65–72. [CrossRef]
20. Tong, Y.; Qiao, J.; Yao, Y. The constitutive model and threshold stress for characterizing the deformation mechanism of $Al_{0.3}$CoCrFeNi high entropy alloy. *Mater. Sci. Eng. A* **2018**, *730*, 137–146. [CrossRef]
21. Tang, Q.; Huang, Y.; Cheng, H.; Liao, X.Z.; Langdon, T.G. The effect of grain size on the annealing-induced phase transformation in an $Al_{0.3}$CoCrFeNi high entropy alloy. *Mater. Des.* **2016**, *105*, 381–385. [CrossRef]
22. Li, D.; Gao, M.C.; Hawk, J.A.; Zhang, Y. Annealing effect for the $Al_{0.3}$CoCrFeNi high-entropy alloy fibers. *J. Alloys Compd.* **2019**, *778*, 23–29. [CrossRef]
23. Gwalani, B.; Gorsse, S.; Choudhuri, D.; Zhang, Y.; Mishra, R.S.; Banerjeeab, R. Tensile yield strength of a single bulk $Al_{0.3}$CoCrFeNi high entropy alloy can be tuned from 160 MPa to 1800 MPa. *Scr. Mater.* **2018**, *162*, 18–23. [CrossRef]
24. Shun, T.; Du, Y. Microstructure and tensile behaviors of FCC $Al_{0.3}$CoCrFeNi high entropy alloy. *J. Alloys Compd.* **2009**, *479*, 157–160. [CrossRef]
25. Choudhuri, D.; Gwalani, B.; Gorsse, S.; Mikler, C.V.; Ramanujan, R.V.; Gibson, M.A.; Bannerjee, R. Change in the primary solidification phase from fcc to bcc-based B2 in high entropy or complex concentrated alloys. *Scr. Mater.* **2017**, *127*, 186–190. [CrossRef]
26. Dasari, S.; Sarkar, A.; Gwalanib, C.; Choudhuri, D.; Soni, V.; Manda, S.; Samajdar, I.; Bannerjee, R. Recovery of cold-worked $Al_{0.3}$CoCrFeNi complex concentrated alloy through twinning assisted B2 precipitation. *Acta Mater.* **2021**, *202*, 448–462. [CrossRef]
27. Gwalani, B.; Torgerson, T.; Dasari, S.; Jajetia, A.; Nartu, M.; Gangireddy, S.; Pole, M.; Wang, T.; Scharf, T.W. Influence of fine-scale B2 precipitation on dynamic compression and wear properties in hypo-eutectic $Al_{0.5}$CoCrFeNi high-entropy alloy. *J. Alloys Compd.* **2020**, *853*, 157126. [CrossRef]
28. Yasuda, H.; Miyamoto, H.; Cho, K.; Nagase, T. Formation of ultrafine-grained microstructure in $Al_{0.3}$CoCrFeNi high entropy alloys with grain boundary precipitates. *Sci. Mater. Lett.* **2017**, *199*, 120–123. [CrossRef]
29. Gwalani, B.; Soni, V.; ChoudHuri, D.; Lee, M.; Hwang, J.; Nam, S.; Ryu, H.; Hong, S.; Banerjee, R. Stability of ordered L12 and B2 precipitates in face centered cubic based high entropy alloys $Al_{0.3}$CoFeCrNi and $Al_{0.3}CuFeCrNi_2$. *Scr. Mater.* **2016**, *123*, 130–134. [CrossRef]
30. Gangireddy, S.; Gwalani, B.; Liu, K.; Banerjee, R.; Mishra, R.S. Microstructures with extraordinary dynamic work hardening and strain rate sensitivity in $Al_{0.3}$CoCrFeNi high entropy alloy. *Mater. Sci. Eng. A* **2018**, *734*, 42–50. [CrossRef]
31. Lu, J.; Li, L.; Zhang, H.; Chen, J.; Luo, L.; Zhao, X.; Guo, F.; Xiao, P. Oxidation behavior of gas-atomized AlCoCrFeNi high-entropy alloy powder at 900–1100 °C. *Corros. Sci.* **2021**, *181*, 190257. [CrossRef]
32. Shun, T.T.; Hung, C.H.; Lee, C.F. The effects of secondary elemental Mo or Ti addition in $Al_{0.3}$CoCrFeNi high-entropy alloy on age hardening at 700 °C. *J. Alloys Compd.* **2010**, *495*, 55–58. [CrossRef]
33. Gwalani, B.; Gangireddy, S.; Zheng, Y.; Song, V.; Mishra, R.S.; Banerjee, R. Influence of ordered L12 precipitation on strain-rate dependent mechanical behavior in a eutectic high entropy alloy. *Nature* **2019**, *9*, 6371. [CrossRef] [PubMed]
34. Gwalani, B.; Pohan, R.; Waseem, O.A.; Alam, T.; Hong, S.; Ryu, H.J. Strengthening of $Al_{0.3}$CoCrFeMnNi-based ODS high entropy alloys with incremental changes in the concentration of Y_2O_3. *Scr. Mater.* **2019**, *162*, 477–481. [CrossRef]
35. Soni, V.; Gwalani, B.; Alam, T.; Dasari, S.; Zheng, Y.; Senkov, O.N.; Miracle, D.; Banerjee, R. Phase Inversion in a Two-phase, BCC+B2, Refractory High Entropy Alloy. *Acta Mater.* **2019**, *185*, 89–97. [CrossRef]
36. Anber, E.; Lang, A.; Lass, E.; Suri, P.K.; Hart, J.L.; Dantuono, D.S.; Diao, H.Y.; Feng, R.; Doherty, R.; Liaw, P.K. Insight into the Kinetic Stabilization of $Al_{0.3}$CoCrFeNi High-Entropy Alloys. *Materialia* **2020**, *14*, 100872. [CrossRef]
37. Kao, Y.; Chen, S.; Chen, T.; Chu, P.C.; Yew, J.W.; Lin, S.J. Electrical, magnetic, and Hall properties of Al_xCoCrFeNi high-entropy alloys. *J. Alloys Compd.* **2011**, *509*, 1607–1614. [CrossRef]
38. Strumza, E.; Hayun, S. Comprehensive study of phase transitions in equiatomic AlCoCrFeNi high-entropy alloy. *J. Alloys Compd.* **2020**, *856*, 158220. [CrossRef]
39. Dasari, S.; Jagetia, A.; Soni, B.; Gwalani, B.; Gorsse, S. Engineering transformation pathways in an $Al_{0.3}$CoFeNi complex concentrated alloy leads to excellent strength-ductility combination. *Mater. Res. Lett.* **2020**, *8*, 399–407. [CrossRef]
40. Dasari, S.; Jagetia, A.; Soni, B.; Gwalani, B.; Gorsse, S.; Banerjee, R. Engineering multi-scale B2 precipitation in a heterogeneous FCC based microstructure to enhance the mechanical properties of a $Al_{0.5}Co_{1.5}CrFeNi_{1.5}$ high entropy alloy. *J. Alloys Compd.* **2020**, *830*, 154707. [CrossRef]

41. Li, Q.; Zhang, T.W.; Qiao, J.W.; Ma, S.; Lu, P.; Xu, B.; Wang, Z. Superior tensile properties of $Al_{0.3}$CoCrFeNi high entropy alloys with B2 precipitated phases at room and cryogenic temperatures. *Mater. Sci. Eng. A* **2019**, *767*, 138424. [CrossRef]
42. Ding, Q.; Zhang, Y.; Chen, X.; Fu, X.; Chen, D.; Chen, S.; Gu, L.; Wei, F.; Bei, H.; Gao, Y.; et al. Tuning element distribution, structure and properties by composition in high-entropy alloys. *Nature* **2019**, *574*, 223–227. [CrossRef] [PubMed]
43. Kurdjumov, G. SACHS G Über den Mechanis Mus der Stählhartung. *Phys. Z* **1930**, *64*, 325–332. [CrossRef]
44. Zhang, Y.; Yang, X.; Liaw, P.K. Alloy Design and Properties Optimization of High-Entropy Alloys. *J. Miner. Met. Mater. Soc.* **2012**, *64*, 830–838. [CrossRef]
45. Singh, S.; Wanderka, N.; Murty, B.S.; Glatzel, U.; Banhart, J. Decomposition in multi-component AlCoCrCuFeNi high-entropy alloy. *Acta Mater.* **2011**, *59*, 182–190. [CrossRef]
46. Guo, S.; Liu, C.T. Anomalous solidification microstructures in Co-free AlxCrCuFeNi$_2$ high-entropy alloys. *J. Alloys Compd.* **2013**, *557*, 77–81. [CrossRef]
47. Tong, C.J.; Chen, Y.L.; Yeh, J.W.; Lin, S.; Shun, T.T.; Tsau, C.H.; Chang, S. Microstructure characterization of Al_xCoCrCuFeNi high-entropy alloy system with multiprincipal elements. *Metall. Mater. Trans. A* **2005**, *36*, 881–893. [CrossRef]
48. Zhao, C.D.; Li, J.S.; Liu, Y.D.; Wang, Y.; Kou, H.; Beaugnon, E.; Wang, J. Tailoring mechanical and magnetic properties of AlCoCrFeNi high-entropy alloy via phase transformation. *J. Mater. Sci. Technol.* **2021**, *73*, 83–90. [CrossRef]
49. Gwalani, B.; Gorsse, S.; Choudhuri, D.; Styles, M.; Zheng, Y.F.; Mishra, R.S.; Banerjee, R. Modifying transformation pathways in high entropy alloys or complex concentrated alloys via thermo-mechanical processing. *Acta Mater.* **2018**, *153*, 169–185. [CrossRef]